applied sciences

MDPI

Article

A Super-Resolution Reconstruction Method for Infrared Polarization Images with Sparse Representation of Over-Complete Basis Sets

Yizhe Ma [1,2,3], Teng Lei [1,2,3], Shiyong Wang [1,3], Zhengye Yang [1,2,3], Linhan Li [1,2,3], Weidong Qu [4] and Fanming Li [1,3,*]

[1] Shanghai Institute of Technical Physics, Chinese Academy of Sciences, Shanghai 200083, China; mayizhe@mail.sitp.ac.cn (Y.M.); leiteng@mail.sitp.ac.cn (T.L.); s_y_w@sina.com (S.W.); yangzhengye20@mails.ucas.ac.cn (Z.Y.); lilinhan@mail.sitp.ac.cn (L.L.)
[2] University of Chinese Academy of Sciences, Beijing 100049, China
[3] Key Laboratory of Infrared Detection and Imaging Technology, Chinese Academy of Sciences, Shanghai 200083, China
[4] Key Laboratory of Electro-Optical Countermeasures Test & Evaluation Technology, Luoyang 471003, China; quwd2013@163.com
* Correspondence: lfmjws@163.com

Abstract: The spatial resolution of an infrared focal plane polarization detection system is limited by the structure of the detector, resulting in lower resolution than the actual array size. To overcome this limitation and improve imaging resolution, we propose an infrared polarization super-resolution reconstruction model based on sparse representation, optimized using Stokes vector images. This model forms the basis for our method aimed at achieving super-resolution reconstruction of infrared polarization images. In this method, we utilize the proposed model to initially reconstruct low-resolution images in blocks. Subsequently, we perform a division by weight, followed by iterative back projection to enhance details and achieve high-resolution reconstruction results. As a supplement, we establish a near-real-time short-wave infrared time-sharing polarization system for data collection. The dataset was acquired to gather prior knowledge of the over-complete basis set and to generate a series of simulated focal plane images. Simulation experimental results demonstrate the superiority of our method over several advanced methods in objective evaluation indexes, exhibiting strong noise robustness in quantitative experiments. Finally, to validate the practical application of our method, we establish a split-focal plane polarization short-wave infrared system for scene testing. Experimental results confirm the effective processing of actual captured data by our method.

Keywords: infrared polarization; super-resolution reconstruction; sparse representation

check for updates

Citation: Ma, Y.; Lei, T.; Wang, S.; Yang, Z.; Li, L.; Qu, W.; Li, F. A Super-Resolution Reconstruction Method for Infrared Polarization Images with Sparse Representation of Over-Complete Basis Sets. *Appl. Sci.* **2024**, *14*, 825. https://doi.org/10.3390/app14020825

Academic Editors: Guoxia Xu and Hu Zhu

Received: 15 December 2023
Revised: 14 January 2024
Accepted: 16 January 2024
Published: 18 January 2024

1. Introduction

With advancements in infrared technology, infrared polarization imaging has found growing applications in various domains, such as industrial inspection [1–3], medical diagnosis [4–6], and astronomical remote sensing [7–9]. This technology facilitates the augmentation of information acquired through infrared imaging and enables further exploration of post-image processing algorithms. The infrared focal plane polarization detector has garnered significant interest as the central component of infrared polarization imaging. It consists of multiple groups of micro-linear polarization units and infrared detectors [10]. The micro-linear polarization units are arranged in an ordered structure on the surface of the infrared detector, with each group containing four pixels. Each group records four different necessary intensity response values [11]. However, this design structure decreases the spatial resolution of the infrared focal plane polarization imaging system, resulting in a significant impact on the measurement accuracy of polarization information. To address the issue of limited sampling by the detector and the inability to obtain a full-resolution polarization image, super-resolution reconstruction of the polarization image is necessary.

This involves utilizing an effective reconstruction algorithm to enhance image details and clarity, compensating for the loss of resolution caused by the system structure.

Super-resolution reconstruction techniques can be categorized based on their implementation methods into interpolation methods [12–16], reconstruction methods [17–19], and learning methods [20–28]. The interpolation methods include bilinear and bicubic interpolation methods [12], which were the initial algorithms utilized for super-resolution tasks. Subsequently, new algorithms were proposed, such as gradient-based interpolation [13], Newton polynomial-based interpolation (NP) [14], Edge-Aware Residual Interpolation (EARI) [15], and polarization image demosaicking using Polarization Channel Difference Prior (PCDP) [16], which leverage image geometric information and channel correlation. These interpolation techniques offer the advantage of quick reconstruction and effective edge preservation. However, since the degradation information of the actual pixel is not always accurately known, the models employed are not fixed.

The primary objective of super-resolution algorithms in reconstruction methods is to reverse-engineer the imaging process of an image. This involves establishing an observation model that links the low-resolution image with the high-resolution image. To solve the model, image-specific prior knowledge is introduced, either at a local or global level. As an example, Chen et al. combined the 3D block-matching algorithm with the concept of non-local filtering and introduced the Block-matching 3D Projectile On Convex Sets (BPOCS) algorithm [17]. Zhang et al. proposed the Frequency domain Phase-based Projection On Convex Sets (FPPOCS) algorithm, which combines the Wiener filter with the phase spectrum features of high-resolution images [18]. Similarly, in our previous work, we utilized principal component analysis and soft threshold denoising, using micro-scanning to capture sub-pixel micro-displacement frame sequences without altering the optical system's structure. We proposed the Micro-scanning Polarization Projection On Convex Sets (MPPOCS) algorithm, designed specifically for infrared focal plane polarization detection systems [19]. The primary focus of the reconstruction method's super-resolution algorithm is the degradation process of the image. It aims to narrow down the range of potential solutions using an observational model, thereby ultimately improving the preservation of the image's geometry. However, due to the complex degradation factors encountered during the imaging process, artificial modeling cannot fully establish this process comprehensively.

The underlying principle of learning methods involves establishing correspondence between low-resolution and high-resolution images, utilizing the complementary information within similar blocks to preserve signal characteristics. In 2018, Zhang et al. introduced the Polarization Demosaicing Convolutional Neural Network (PDCNN) [20] to address the challenge of polarization super resolution, which lacked a specialized network for focal plane polarizing images. Subsequently, to mitigate accumulated errors caused by formula computation steps, Zeng et al. proposed an end-to-end fully convolutional neural network, FORK-NET [21]. This network takes the focal plane image as input and generates output intensity, polarization degree, and polarization angle images. An objective evaluation index indicated the superior performance of FORK-NET compared to PDCNN. Consequently, researchers explored alternative network models, such as the Multi-Scale Adaptive Weighted Network (MSAWN) [22], Deep Compressed Sensing (DCS) [23], and the sparsely polarimetric image demosaicing model (Sparse-PDM) [24]. These networks primarily target visible light polarization and necessitate extensive training data, typically sourced from Sony IMX250 series visible light polarization cameras. Articles [24,25] describe the publicly available dataset created by these researchers. The advantage of deep learning methods lies in their ability to achieve excellent reconstruction effects. Nevertheless, these methods also possess certain drawbacks that limit their suitability for specific tasks. Super-resolution performance becomes heavily reliant on computational power and data volume, limiting their deployment in computationally constrained and data-limited environments. Furthermore, the lack of clear interpretation in the structural units is evident. Conversely, shallow learning methods derived from traditional machine learning algorithms offer advantages such as adaptability to small datasets, relatively lower computational costs, and interpretability.

In this paper, we propose an infrared polarization super-resolution reconstruction model based on sparse representation. Our model optimizes the Stokes vector images, eliminating the need for mechanical reconstruction of a multi-channel polarization image. To enhance efficiency and accuracy, we construct three over-complete sets of Stokes vector image dictionaries. These dictionaries streamline the calculation process of the polarization degree and polarization angle while minimizing the potential for error.

Furthermore, we introduce a reconstruction method based on our model. This method utilizes the proposed model to initially reconstruct the low-resolution image in blocks. The image is then divided by the weight coefficients of the overlaps, and the details are refined using the Iterative Back Projection (IBP) technique to achieve high-resolution reconstruction results.

To build the dictionary, we designed a near-real-time short-wave infrared time-sharing polarization system prototype, leveraging our previous error analysis work [29]. This prototype enabled us to acquire the necessary dataset for simulation experiments. Additionally, we established a short-wave infrared focal plane polarization system for capturing real data. The experimental results demonstrate the superiority of our proposed method in both objective and subjective evaluation indexes.

The rest of this paper is organized as follows: Section 2 introduces the reconstruction model and algorithm, including the establishment of an over-complete dictionary set, noise analysis, and the iterative solution method. Section 3 presents the simulation and real experiment results, provides the objective evaluation index, and explains the subjective index. The anti-noise performance of the proposed algorithm is analyzed, and the running time of the algorithm is provided. Next, we discuss the results and introduce future research directions. Finally, Section 4 discusses the advantages of the proposed method, summarizes the novelty of the method and our contributions, and describes future research direction.

2. Super-Resolution Methods

An infrared focal plane detection system can capture essential intensity images from four different angles in a single exposure. Due to limitations imposed by the detector structure, the effective resolution of the four declination angle images is reduced by half of the original pixel size, expressed mathematically as follows:

$$I_{\theta_{i=1,2,3,4}}^{\mathrm{M}/2\times\mathrm{N}/2} = I_{\mathrm{out}}^{M\times N} * \mathrm{Mask}_{\theta} \tag{1}$$

where $I_{\mathrm{out}}^{M\times N}$ represents the cumulative light intensity recorded by the detector, analogous to an image obtained from a single exposure at a specific angle. $Mask_{\theta}$ is an intensity extraction mask that biases the detection process to isolate the individual angle components within the overall light intensity. This mask is dependent on the pixel arrangement employed by the self-developed detector. Each superpixel within this arrangement consists of a tuple of four pixels. The resulting separated images for each declination angle, denoted as $I_{\theta_{i=1,2,3,4}}^{\mathrm{M}/2\times\mathrm{N}/2}$, exhibit a reduced size of half the original dimensions. The Stokes notation is a widely utilized method for representing polarization states in engineering, and its formula is provided below:

$$\mathbf{S} = \begin{bmatrix} S0 & S1 & S2 & S3 \end{bmatrix} \tag{2}$$

where $S0$, $S1$, $S2$, and $S3$ are parameters that describe different aspects of the incident light. $S0$ represents the total incident light intensity. $S1$ is the difference in intensity between the horizontal and vertical directions. $S2$ is the intensity difference between polarized light at 45 degrees and 90 degrees concerning a reference direction. $S3$ specifically relates to the detection of left-handed versus right-handed circular polarization. In typical projects, the detection of linear polarized light is generally carried out without considering the $S3$ component. By using the above formula, it is possible to solve for the Stokes vector of the incident light inversely. This method allows for the retrieval of information about the polarization degree and polarization angle of the current scene.

$$DP = \frac{\sqrt{S1^2 + S2^2}}{S0} = \frac{\sqrt{(I_0 - I_{90})^2 + (I_{45} - I_{135})^2}}{(I_0 + I_{45} + I_{90} + I_{135}) \times \frac{1}{2}} \tag{3}$$

$$AP = \frac{1}{2}\arctan(\frac{S2}{S1}) = \frac{1}{2}\arctan(\frac{I_{45} - I_{135}}{I_0 - I_{90}}) \tag{4}$$

When $I_{\theta_{i=1,2,3,4}}^{\mathrm{M}/2\times\mathrm{N}/2}$ is directly included in the aforementioned calculation formula, it becomes apparent that the dimensions of DP and AP calculated in this manner are $M/2 \times N/2$. Furthermore, due to the unique arrangement structure of the superpixel, only a single declining-angle light intensity of a given pixel can be obtained in a single exposure. This leads to an instantaneous field error in the calculated polarization signal. Hence, it is imperative to conduct super-resolution reconstruction of $I_{\theta_{i=1,2,3,4}}^{\mathrm{M}/2\times\mathrm{N}/2}$.

2.1. Infrared Polarization Super-Resolution Reconstruction Model

To obtain the high-resolution image I_{SR}, the low-resolution image I_{LR} is used. It is assumed that I_{SR} can be linearly represented as α using the over-complete basis vector space D_{SR}. According to the theory of root sparse coding primitives, we can infer that the following formula holds when α is sufficiently sparse:

$$\widetilde{I}_{SR} = D_{SR}\alpha \quad \exists\alpha \in \mathbf{R^k} \; with \; \|\alpha\|_0 << k \tag{5}$$

The over-complete basis vector D_{SR}, which can also be referred to as an over-complete dictionary set, is utilized. The objective is to minimize the Euclidean distance between the reconstructed image $\widetilde{I}_{SR}$ and the actual high-resolution image, while ensuring that α satisfies the sparsity condition. This can be formulated as an optimization problem:

$$\min_a \|\alpha\|_0 \quad s.t. \quad \|D_{SR}\alpha - I_{SR}\|_2^2 < \varepsilon \tag{6}$$

Formula (6) satisfies the condition that the square of the 2-norm is smaller than the error ε, rather than just the 2-norm being smaller than the error ε. This choice is justified by previous research which has shown that in the field of super-resolution reconstruction, penalizing high-frequency errors by using the square of the 2-norm yields better results [26–28]. When performing super-resolution tasks with the input of image I_{LR}, it is evident that Formula (6) does not have enough known optimization solutions. In this context, the existence of dictionary D_{LR} is assumed. This dictionary shares the sparse representation α with D_{SR}, and solving Formula (6) can be equivalently stated as the following equation:

$$\min_a \|\alpha\|_0 \quad s.t. \quad \|GD_{LR}\alpha - GI_{LR}\|_2^2 < \varepsilon \tag{7}$$

In the equation above, G denotes an edge extraction operator, responsible for generating edge features for Formula (7). We observe that the pseudo-polarization information is primarily concentrated in the high-frequency portion. Precisely reconstructing the missing high-frequency content in the targeted high-resolution image holds the utmost significance. Extracting the high-frequency components from low-resolution images proves advantageous for the reconstruction of high-resolution images [30]. Formula (7) corresponds to an L0 problem, which can be approximated through an L1 problem using the Lagrange multiplier method:

$$\min_a \|GD_{LR}\alpha - GI_{LR}\|_2^2 + \lambda\|\alpha\|_1 \tag{8}$$

In Formula (8), λ is an adjustable parameter that is associated with the noise variance of the input image I_{LR}. The derivation process will be conducted later on. With the given image I_{LR} and over-complete dictionary sets D_{SR} and D_{SR}, a set of optimal sparse representations α^* is obtained by solving Formula (8). Subsequently, the reconstructed image $\widetilde{I}_{SR}$ can be obtained by applying it to Formula (5). The resulting image satisfies the constraint stated in Formula (6).

We introduce adjustable parameter λ into Formula (8), which is derived and analyzed using the Maximum A Posteriori (MAP) theory. According to the MAP theory, the squared term of the L2 norm in Formula (8) can be interpreted as the maximum likelihood estimate of α. Additionally, part of the L1 norm can be considered as the Laplace prior of α. Without taking into account the edge extraction operator G, this prior can be expressed as follows:

$$\alpha^* = \mathrm{ar}\underset{\alpha}{g}\max\ p(I_{LR} \mid D_{LR}, \alpha)p(\alpha) \tag{9}$$

The α variable in Formula (9) follows a Laplace distribution with the parameter (0, b). As a result, its probability density function can be expressed as follows:

$$p(\alpha) = \frac{1}{2b}e^{-\frac{|\alpha|_1}{b}} \tag{10}$$

The variable I_{LR} in Formula (9) is distributed according to a Gaussian distribution with the parameter $\left(D_L a, \delta^2\right)$. Thus, its probability density function can be expressed as follows:

$$p(I_{LR} \mid D_{LR}, \alpha) = \frac{1}{\sqrt{2\pi}\delta}e^{\frac{1}{-2\delta^2}\|D_{LR}\alpha - I_{LR}\|_2^2} \tag{11}$$

By incorporating Formulas (10) and (11) into Formula (9), we derive the resulting Formula (12):

$$\begin{aligned}\alpha^* &= \arg\max_{\alpha} \log p(I_{LR} \mid D_{LR}, \alpha) + \log p(\alpha) \\ &= \arg\max_{\alpha} \tfrac{1}{-2\delta^2}\|D_{LR}\alpha - I_{LR}\|_2^2 + \tfrac{1}{-2b}|\alpha|_1 \\ &= \arg\min_{\alpha} \|D_{LR}\alpha - I_{LR}\|_2^2 + \tfrac{\delta^2}{b}|\alpha|_1\end{aligned} \tag{12}$$

Equation $\lambda = \delta^2/b$ can be observed from the aforementioned formula. Given the sparsity of α, it is assumed that the scale parameter b remains relatively constant, while λ should be increased in the presence of higher input image noise. For the experiment, a value of 0.2 was assigned to λ.

2.2. Reconstruction Method

$I_{\theta_{i=1,2,3,4}}^{\mathrm{M}/2\times\mathrm{N}/2}$ is a low-resolution image. If $I_{\theta_{i=1,2,3,4}}^{\mathrm{M}\times\mathrm{N}}$ in the same scene is solved, the DP and AP of full-resolution images can be solved using Formulas (3) and (4). Consequently, the Stokes vector needs to be calculated. The calculation process involves finding the difference between two groups of orthogonal light intensities. It is important to note that the different image is significantly influenced by the displacement of the target. Based on the experimental findings in [19], displacement-induced pseudo-polarization has a substantial impact on subjective perception. Therefore, our reconstruction method is expressed in the following equation:

$$\begin{aligned}&\alpha^* = \arg\min_{a}\|\alpha\|_0\ \ S.T.\quad \|GD_{LR}\alpha - GI_{LR}\|_2^2 < \varepsilon \\ &I_{LR} = \{S0_{LR}, (S1/S0)_{LR}, (S2/S0)_{LR}\} \\ &I_{SR} = D_{SR}\alpha^*\end{aligned} \tag{13}$$

$S0_{LR}$ is reconstructed as $S0_{SR}$ through the use of super resolution. Subsequently, $(S1/S0)_{LR}$ and $(S2/S0)_{LR}$ are reconstructed as $(S1/S0)_{SR}$ and $(S2/S0)_{SR}$, respectively. Finally, the DP and AP images at full resolution are calculated. This reconstruction approach offers several benefits. First, it eliminates the need to calculate the difference between each angular component, thereby avoiding any potential angle errors. Additionally, the reconstruction of $(S1/S0)_{SR}$ and $(S2/S0)_{SR}$ does not rely on the light intensity of the scene.

The light intensity captured by the detector encompasses both natural and fully polarized light components, which can be derived using Malus' law:

$$I^{\theta} = \frac{1}{2} I_N + I \times P \times \cos^2(\theta - A) \tag{14}$$

In the formula above, I^{θ} represents the intensity of partially polarized light at a given declination angle θ. This can also be interpreted as the light intensity received by the detector at that angle. I^N represents natural light, while I^N represents the total light intensity. I^N denotes the degree of polarization, while A represents the polarization angle. The orthogonal difference of polarization is defined [31] as:

$$I_{\perp}^{\theta} = I_{\perp}^{\theta} - I_{\perp}^{\theta+\frac{\pi}{2}} = I(1-P) \times (\cos^2(\theta - A) - \cos^2(\frac{\pi}{2} + \theta - A)) \tag{15}$$

In the formula above, when $\theta = 0^{\circ}$, $I_{\perp}^{\theta} = S1$, and $\theta = 45^{\circ}$, $I_{\perp}^{\theta} = S2$. The Stokes representation of the total light intensity I is denoted as $S0$. Therefore, $(S1/S0)_{LR}$ and $(S2/S0)_{LR}$ are influenced by the polarization degree and polarization angle. By reconstructing them, it is possible to achieve better restoration of the DP and AP images at full resolution, instead of directly reconstructing the DP and AP low-resolution images from the high-resolution $S0$, DP, and DP images. The proposed method does not take the entire image as input. Instead, a sliding window reconstruction is performed on a low-resolution image. The window size is set at 5×5, with a step length of 1. During the reconstruction process, the number of overlapping pixels is calculated, and the reconstructed $\widetilde{I}_{SR}$ is divided by the overlap coefficient W. The operational details are presented in the figure below.

As shown in Figure 1, the red segment illustrates a pixel-level reconstruction process where each pixel is reconstructed once, using a weight factor of $W = 1$. The yellow part represents another reconstruction process. It is important to clarify that this specific depiction of traversing during the second step is not obligatory, as any traversal with a step size of 1 covering the entire image would be sufficient. It is worth noting that there is an overlap between the yellow and red segments. In terms of pixel-level analysis, the overlapping region carries a weight coefficient of $W = 2$. The resulting reconstructed I_{SR} is then divided by the overlap coefficient W. Additionally, the Iterative Back Projection (IBP) algorithm is employed to enhance image details and minimize the reconstruction error of the reconstructed $\widetilde{I}_{SR}$. The input for the IBP algorithm is composed of the reconstructed image $\widetilde{I}_{SR}$ and the reference image obtained through the sampling of I_{LR} using the bicubic interpolation method.

The overall method consists of the following steps:

(1) The acquired low-resolution image is initially divided into sliding window blocks with a step size of 1 and window size of 5×5.
(2) The α^* of each component is solved using Formula (8), and in this process, the feature symbol search algorithm proposed in [32] is employed.
(3) The reconstructed image $\widetilde{I}_{SR}$ of each component is then divided by the overlap coefficient W.
(4) The Iterative Back Projection (IBP) algorithm is used to further reconstruct each component's W.
(5) Finally, the Stokes vector image, polarization degree image, and polarization angle image are calculated based on the reconstructed results.

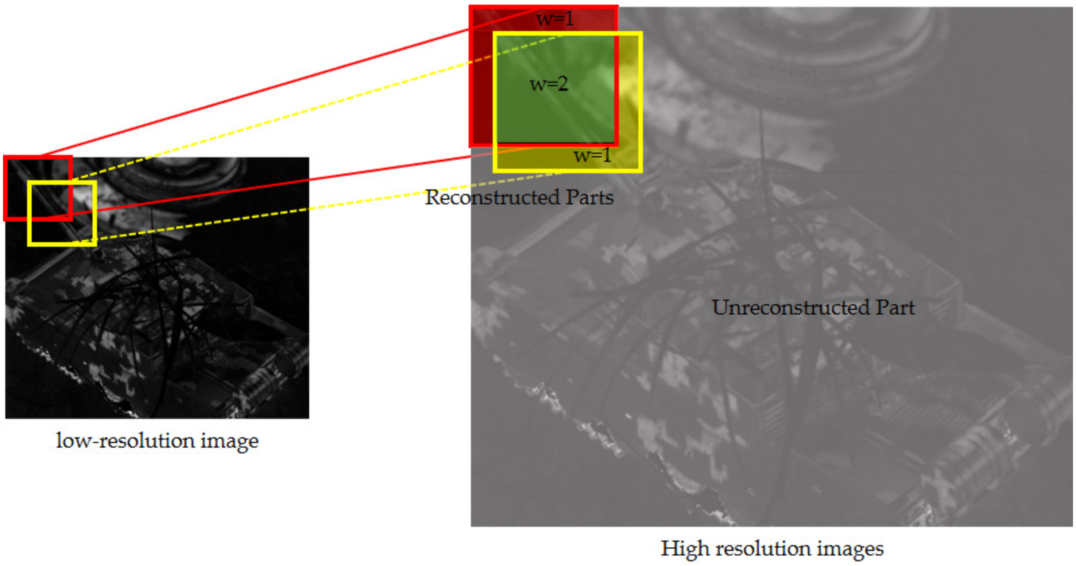

Figure 1. Change in the overlap coefficient in the sliding window super-resolution process. The red window represents one step of the rebuilding process, while the yellow window represents another step. The overlapping portion carries a weight of 2, whereas the non-overlapping section holds a weight of 1.

2.3. Establishment of Dictionary Set

Section 2.1 discusses the dictionary, called D_{LR}, which is mentioned as having a shared sparse representation with D_{SR}. To achieve our desired solution, we need to construct a joint dictionary. The optimization problem for this joint dictionary is represented in the downward form:

$$\min_{D_{LR},D_{SR},\alpha_U} \frac{1}{C_1}\|GD_{LR}\alpha_U - GT_{LR}\|_2^2 + \frac{1}{C_2}\|D_{SR}\alpha_U - T_{SR}\|_2^2 + \lambda(\frac{1}{C_1} + \frac{1}{C_2})|\alpha_U|_1 \tag{16}$$

The variables C_1 and C_2 in the formula above are used to balance the costs of the Dictionary-based Super-Resolution D_{SR} and Dictionary-based Low-Resolution D_{LR} methods. Since the reconstruction method requires a sliding window, the dictionary set is also built using a sliding window approach with a window size of 5 and step size of 1. However, this practice leads to inconsistent matrix sizes, so we up-sample the low-resolution image before building the dictionary set. The values of C_1 and C_2 are set to the number of atoms corresponding to D_{LR} and D_{SR}, respectively. In our case, C_2 is set to 25 and C_1 is set to 100, as our edge extraction operator G is defined as the first and second derivatives in the x and y directions. Additionally, we further simplify Formula (16):

$$\begin{gathered} \min_{D_U,\alpha_U} \|D_U\alpha_U - T_U\|_2^2 + \lambda|\alpha_U|_1 \\ D_U = \begin{bmatrix} \frac{1}{10}GD_{LR} \\ \frac{1}{5}D_{SR} \end{bmatrix} \qquad T_U = \begin{bmatrix} \frac{1}{10}GT_{LR} \\ \frac{1}{5}T_{SR} \end{bmatrix} \end{gathered} \tag{17}$$

According to [33], to optimize the problem of solving Formula (17), it is necessary to constrain D_U. This ensures the existence of both $\mathrm{d}_{\mathrm{U,i}}^{\mathrm{rank}\ (D_U)\times 1}$ and α_U atomic sets within D_U, which leads to consistent results for $\mathrm{d}_{\mathrm{U,i}}^{\mathrm{rank}\ (D_U)\times 1} \cdot \alpha_U$ and approaching 0 for $|\alpha_U|_1$. As a result, it is crucial to normalize the atomic sets of D_U and impose constraints before training. Representation of the entire dictionary set can be expressed using the following formula, with K being the total number of atomic sets in the dictionary set, set to 512 during training:

$$D_U^* = \underset{D_U,\alpha_U}{\operatorname{argmin}}\|D_U\alpha_U - T_U\|_2^2 + \lambda|\alpha_U|_1 \quad \text{s.t.} \left\| d_{u.i}^{rank(\alpha_U)*1} \right\|_2^2 \leq 1, i = 1,2,3,\ldots K \tag{18}$$

The formula is not convex on both D_U and α_U. However, it is convex on one of them. To address this, we follow the approach proposed in [32]. We first initialize D_U and solve α_U using the feature symbol search algorithm. Then, we fix α_U and solve the duality problem of α_U using the conjugate gradient method. Solving the duality problem offers the advantage of generating fewer variables during the optimization process, thus making it faster.

3. Results

To validate the proposed method, we created a prototype near-real-time short-wave infrared time-sharing polarization system for collecting training and simulation data, building upon our previous work. As shown in Figure 2. The system utilized a custom short-wave detector that operated within the 0.95~1.65 µm wavelength range. Additionally, a self-designed zoom lens with a resolution of 120 lp/mm was employed. Real-time communication with the host optical signal was facilitated by the fully electronic design of the rotating target wheel component. The system offered a polarization time resolution of 25 frames. A total of 60 scenes, encompassing indoor and outdoor settings, were captured. Amongst these scenes, 54 were used to form the training dictionary set, while 6 scenes were reserved for simulation testing. The $S0$ images from the simulation test are depicted in Figure A1 in Appendix A, showcasing cars, a window, a wall, a building, a tower, and a tank. Each image has a resolution of 640 × 512 pixels.

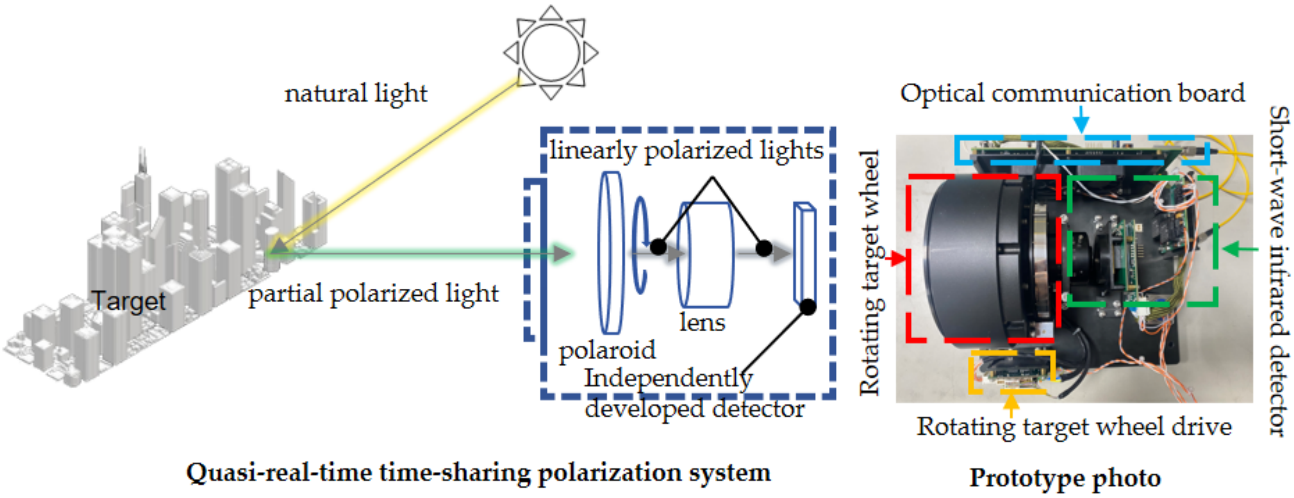

Figure 2. Production of the near-real-time short-wave infrared time-sharing polarization system. In our study, the incident natural light is partially polarized when it reflects off the target. Subsequently, it passes through a polarizer to obtain linear polarization. The linearly polarized light then travels through the lens and reaches the shortwave infrared detector. In terms of the physical products we manufactured, the foremost component was a motor-controlled rotating target wheel. We achieved high-precision angle control using a grating ruler. The entire system was connected to the upper computer via fiber optics for transmission.

In this paper, four interpolation methods were utilized: the Newton polynomial-based interpolation method (NP) [14], the Edge Sensing Residual Interpolation method (EARI) [15], a polarization difference priority-based interpolation algorithm (PCDP) [16], and the Micro-scanning Polarization Projection On Convex Sets (MPPOCS) algorithm [19], which we previously proposed. As the MPPOCS algorithm is a multi-frame super-resolution algorithm, we modified its input. In the simulation experiment, we simulated the micro-scan image input using a single frame image. For the real image test, we directly employed a multi-frame image as the input.

In terms of objective evaluation indicators, three commonly used methods in super-resolution reconstruction tasks were selected: a structural similarity coefficient (SSIM), the Peak Signal-to-Noise Ratio (PSNR), and Root Mean Square Error (RMSE). These evaluation criteria were applied to the normalized images of $S0$, $S1$, $S2$, DP, and AP, respectively. A higher SSIM indicated that the reconstructed image closely resembled the reference image in terms of intensity, contrast, and structure. The accuracy of each polarization component's reconstructed image reflected the true polarization characteristics of the object. The noise in the polarization image mainly manifested as false polarization. PSNR, which measures the ratio of peak signal energy to average noise energy, was used to assess the pseudo-polarization level in each component of the reconstructed polarization image. RMSE was used to gauge the degree of similarity between the reconstructed polarization image and the true polarization image in terms of pixel position. A smaller RMSE value indicated a closer match between the reconstructed and true polarization values for the same pixel position. By combining these three objective evaluation measures with subjective criteria, a comprehensive analysis of the proposed reconstruction method was conducted.

3.1. Super-Resolution Performance Test

The experimental setup consisted of a PC host with an i7-4720HQ CPU (Intel Corporation, Santa Clara, CA, USA) and GTX960 GPU (Nvidia Corporation, Santa Clara, CA, USA). The specific parameter settings for both the reconstruction and training parts of the dictionary set are provided and explained in Section 2. It is important to note that dictionary set learning takes place after the image segmentation process. For training purposes, we randomly selected 100,000 windows from 54 training scenes, each with dimensions of 5×5. No noise reduction algorithm was employed following the non-uniformity correction and blind element repair of the captured images. Consequently, the resulting images may have contained electronic noise, dark current noise [34], stray light response, and some uncorrected blind elements. The objective evaluation indicators for the simulation results are depicted in Table 1.

Table 1. The objective evaluation indexes of each algorithm for a tower.

Method	S0	S1	S2	DP	AP
EARI	SSIM = 0.9649 PSNR = 35.6509 RMSE = 0.0165	SSIM = 0.9670 PSNR = 41.4362 RMSE = 0.0085	SSIM = 0.9751 PSNR = 42.4668 RMSE = 0.0075	SSIM = 0.8148 PSNR = 27.9892 RMSE = 0.0399	SSIM = 0.7559 PSNR = 19.8982 RMSE = 0.1012
NP	SSIM = 0.9708 PSNR = 36.8702 RMSE = 0.0143	SSIM = 0.9807 PSNR = 43.5596 RMSE = 0.0066	SSIM = 0.9842 PSNR = 44.0752 RMSE = 0.0063	SSIM = 0.8599 PSNR = 29.7688 RMSE = 0.0324	SSIM = 0.7749 PSNR = 23.2195 RMSE = 0.0690
PCDP	SSIM = 0.9723 PSNR = 37.1946 RMSE = 0.0138	SSIM = 0.9748 PSNR = 42.4574 RMSE = 0.0075	SSIM = 0.9827 PSNR = 43.67161 RMSE = 0.0066	SSIM = 0.8512 PSNR = 29.2385 RMSE = 0.0345	SSIM = 0.7602 PSNR = 22.4482 RMSE = 0.0754
MPPOCS	SSIM = 0.9687 PSNR = 36.1099 RMSE = 0.0156	SSIM = 0.9972 PSNR = 54.8412 RMSE = 0.0018	SSIM = 0.9952 PSNR = 50.9966 RMSE = 0.0028	SSIM = 0.9610 PSNR = 38.9372 RMSE = 0.0113	SSIM = 0.9452 PSNR = 38.6978 RMSE = 0.0116
This Work	SSIM = 0.9809 PSNR = 40.0757 RMSE = 0.0099	SSIM = 0.9980 PSNR = 56.8644 RMSE = 0.0014	SSIM = 0.9972 PSNR = 54.0460 RMSE = 0.0019	SSIM = 0.9729 PSNR = 41.8172 RMSE = 0.0081	SSIM = 0.9595 PSNR = 41.3630 RMSE = 0.0086

The table above clearly demonstrates the excellent reconstruction performance achieved by the proposed method. All five algorithms yielded good results for the $S1$ and $S2$ images. The majority of pixels in the $S1$ and $S2$ images represented the low-frequency component. Despite this, our approach still stood out and achieved the best results. Unlike the other algorithms, our method did not obtain the $S1$ and $S2$ images by detecting the difference in declination angle. On the $S0$ index, the MPPOCS method exhibited a low reconstruction effect. This is because the filtering method used in this algorithm sacrifices some details of the decline-detecting image, reduces the noise of the orthogonal difference image, and neglects the quality of the weighted image. In our reproductions of the other algorithms, some did not align with the original data. We analyzed these replications in our experiments using the publicly available source code provided by the original authors. The primary difference lay in the down-sampling technique. The authors used interlaced pixel extraction for the simulation, resulting in simulated images with minimal noise. In contrast, our simulated image contained significantly more noise. Additionally, our degradation process employs bicubic interpolation to obtain the subsampled image, where the pixels in the neighborhood are double cubic-weighted. This is because we considered that one of the imaging units of the detector does not correspond one-to-one with the real scene, as it contains a weighted component from the neighborhood due to the system's point spread function. The impact of calculation errors was evident in the DP and AP indexes. If one of the Stokes vector images exhibited unsatisfactory reconstruction, the objective indexes of DP and AP were greatly diminished. In other words, the DP and AP images were more susceptible to noise. Therefore, it was crucial to analyze the noise robustness of the method, and a detailed experimental analysis will be presented in the next section. Figure 3 showcases the simulation reconstruction results of the different algorithms for a tower, where it is evident that the proposed method yielded results closer to the real image. Additionally, Table A1 in Appendix A displays the objective index of $S0$ after the reconstruction of other test images, while Table A2 presents the objective indicators of $S1$, and Table A3 exhibits the objective indicators of $S2$. Furthermore, Table A4 provides the objective index of DP, and Table A5 presents the objective index of AP after the reconstruction of other test images.

3.2. Noise Robustness

Limited by the manufacturing process of the detector, the noise of a focal plane polarization system is generally higher than that of a time-sharing polarization system. Therefore, it was crucial to analyze the noise robustness of the algorithm. Based on the comparison results presented in the previous section, both the proposed method and MPPOCS outperformed other methods. Consequently, this section compares the noise robustness between these two methods. The test image again was a tower. Gaussian white noise with mean 0 and standard deviation ranging from 0 to 3 was added to the focal plane image synthesized by each bias detection component of the tower. The value of λ, introduced in this paper, was set to 0.02. The objective indexes for the reconstructed $S0$ and DP images of the two algorithms are depicted in Figure 4, while the reconstructed indexes for the $S1$, $S2$, and AP images are shown in the attached Figures A2 and A3a,b. SSIM is represented on the black axis, PSNR on the intermediate axis, and RMSE on the blue axis. The + line represents the algorithm proposed in this paper, and the $\times$ line represents MPPOCS.

In Figure 4a, the objective evaluation index of the proposed algorithm gradually decreased as the level of noise increased, with a decline rate higher than that of MPPOCS. In Figure 4b, when the mean noise was 0.9, the SSIM index of our proposed method started to become lower than that of MPPOCS. When the mean noise values were 2.7 and 2.8, respectively, both PSNR and RMSE were weaker than those of the MPPOCS algorithm. Similar results were observed for the $S1$, $S2$, and AP images. In this set of experiments, we kept the λ values unchanged. These findings proved that the proposed algorithm possessed inherent noise resistance, as the reconstruction results were superior to MPPOCS when the noise level was low. Additionally, our algorithm demonstrated better performance in the case of low noise, as shown in Figure 4a. This can be attributed to the fact that the $S0$ image was less sensitive to the noise in each channel compared to the other components, resulting in consistently optimal reconstruction results. We analyzed the results to ascertain the reasons behind the MPPOCS algorithm's high noise robustness. The inclusion of wavelet threshold noise reduction in the algorithm grants it a natural adaptability to noise, especially in the presence of high levels of noise. However, in the context of weak noise, this can lead to excessively smooth image results, as illustrated in Figure 3.

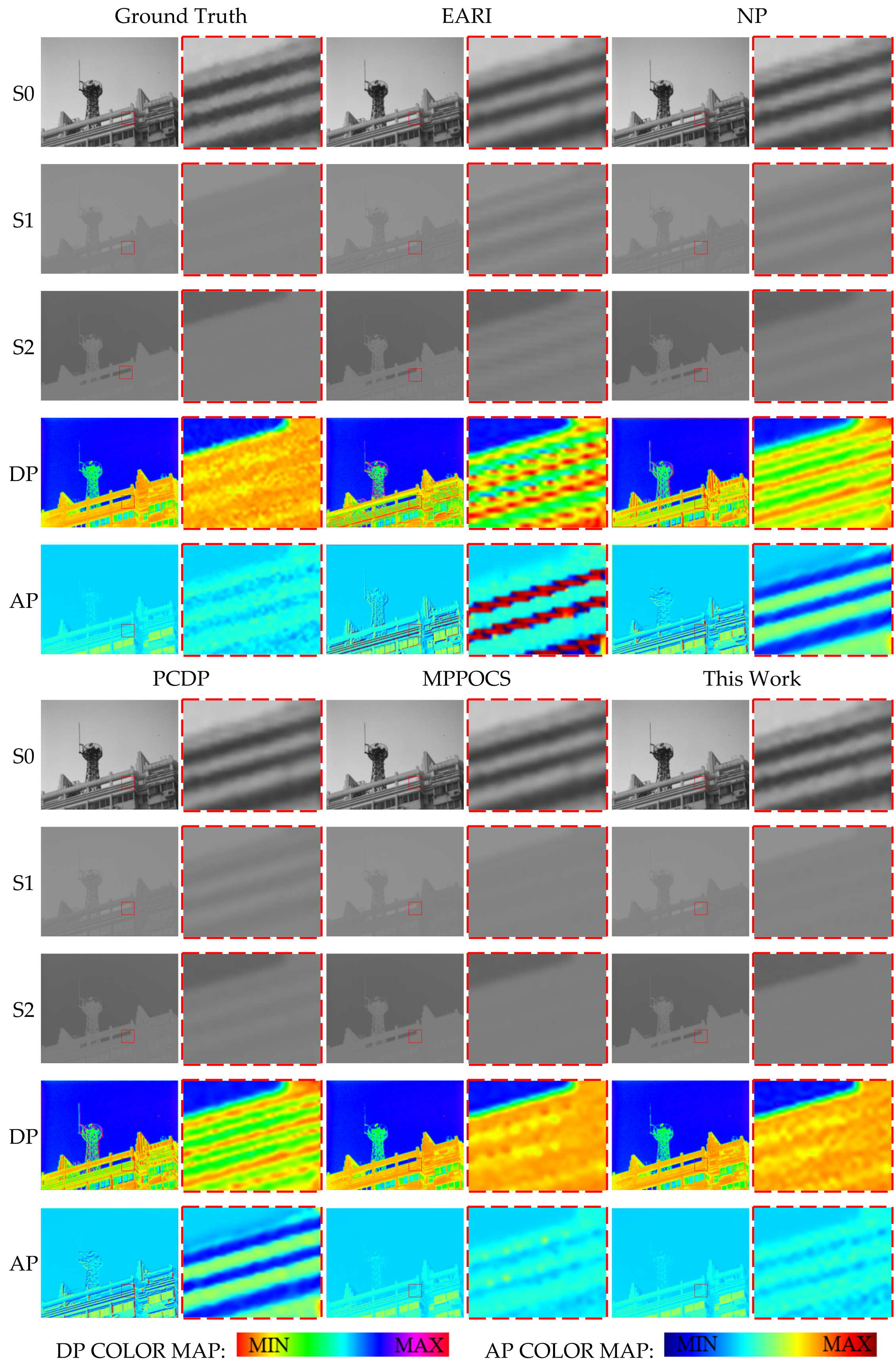

Figure 3. The simulation reconstruction results of each algorithm for a tower. The ground truth image provides a high-resolution representation of each image. The EARI algorithm exhibits a notable false

bias in the AP and DP images, and the S0 image appears blurred. Additionally, the edge details show a noticeable jagged appearance. Both the NP and PCDP algorithms display clear high-frequency errors in the reconstructed S1 and S2 images, as they rely on a set of orthogonal polarization angle image differences to obtain these components. When compared with the ground truth's S1 and S2 images, it is evident that these two methods yield larger errors. Although visually improved, the DP and AP images reconstructed by the NP and PCDP algorithms display sharp edges resulting from pseudo-polarization effects. Due to the strong noise reduction algorithm used in the MPPOCS algorithm, some loss of detail is observed, leading to a relatively fuzzy reconstruction of the S0 image. Our proposed algorithm achieves a close resemblance to the ground truth in terms of the S1 and S2 images; however, it also captures additional details in the AP and DP images compared to the MPPOCS algorithm.

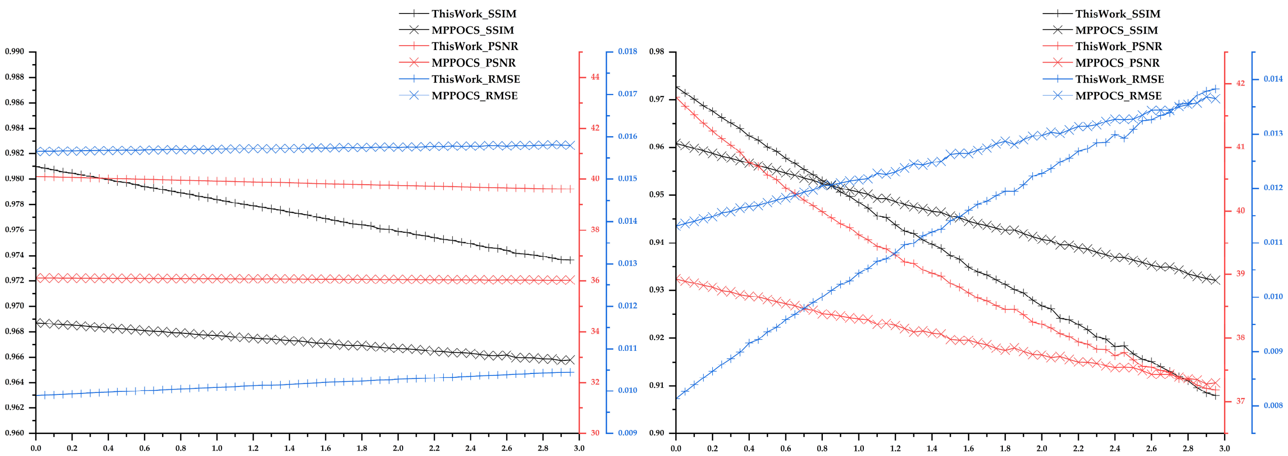

(**a**) (**b**)

Figure 4. The objective evaluation indexes of our algorithm and MPPOCS for a tower, as measured under varying noise conditions. (**a**) Objective evaluation indexes of S0. (**b**) Objective evaluation indexes of DP.

3.3. Real Image Testing

We established a focal plane polarization detection system operating in the short-wave infrared range to collect real images to test our algorithm. The size of the focal plane images was 320 × 256 pixels. The obtained test results are shown in Figure 5.

The selected test scene had cloudy weather conditions. The drone used as the target was the DJI Spirit 4Pro (DJI, Shenzhen, China). All display results were normalized to the same quantization level. No additional image enhancement algorithms were applied to the presentation results. Figure 5 shows the full-field $S0$ image, revealing a dim target. Among the various algorithms tested, the EARI algorithm produced the fuzziest $S0$ image. In several other channels, it was not possible to identify the target as a drone. However, some areas of the DP image allowed for the calculation of the degree of polarization. The NP and PCDP algorithms did not clearly show the target in the $S1$ image. In the DP image, neither of these two algorithms accurately calculated the polarization degree of the UAV. Man-made objects, being more polarized than the natural background, did not exhibit this phenomenon well in the results. These two algorithms introduced significant errors in the AP images. Due to the drone's orientation towards the lens, the polarization angles of its left and right sides did not significantly differ. As for MPPOCS, it can be observed that the $S0$ image was overly blurry. The filter utilized in this algorithm reduced noise in the entire image, but it also sacrificed some high-frequency information. The $S1$ and $S2$ images performed better than with the NP and PCDP algorithms. The DP image provided a clearer representation of the target's polarization information compared to the EARI algorithm. The AP image was slightly more distinct than with the first three algorithms.

Ultimately, our proposed $S0$ algorithm yielded the best results for the image. The brackets on the left and right holding the rotors were separated from the drone's fuselage. The $S1$ and $S2$ images outperformed other algorithms, particularly in the AP image, where our proposed algorithm accurately reconstructed the entire shape of the UAV. With a certain level of prior knowledge, the UAV could be identified as the DJI Genie 4Pro drone even without specialized equipment. Additionally, in the DP image, our reconstruction results displayed the target's polarization degree. The target's edges were sharp, and the difference between the target and background was highly noticeable, providing a strong foundation for the recognition of small polarized targets. Finally, the processing time of the proposed algorithm was statistically analyzed and is shown in Table 2.

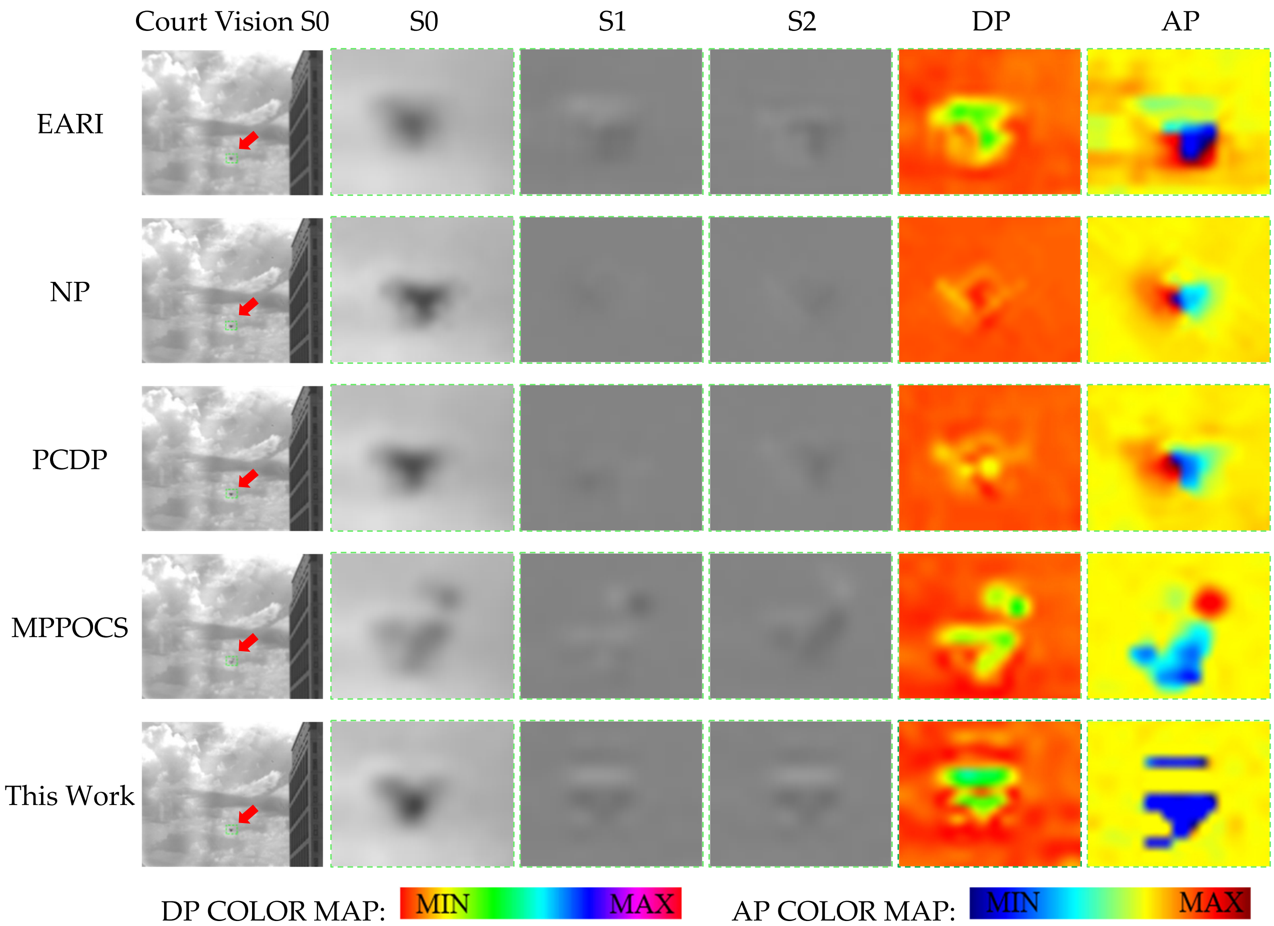

Figure 5. Real scene reconstruction results of each algorithm. Our algorithm achieved good performance in image processing. In the S0 image, the body of the unmanned aerial vehicle is distinguished from the fixed rotor support structures on its sides. Our algorithm effectively restored the form of the unmanned aerial vehicle. Even without specialized equipment, we were capable of visually recognizing the target. In the AP and DP images, our reconstruction results distinctly demonstrate the polarization degree of the target. The target's edges are clearly visible, and there is a noticeable contrast between the target and background. Our algorithm provides a reliable foundation for identifying small polarized targets.

Table 2. The real image reconstruction results of each algorithm's running time.

Method	EARI	NP	PCDP	MPPOCS	This Work
Running Time/s	0.31	0.19	0.03	1.18	18.84

The running time of the method proposed in this paper appeared to be relatively long, as shown in Table 2. To analyze the source code, we employed MATLAB's runtime analysis tool. Our analysis revealed that the feature symbol search algorithm accounted for a significant portion of the computing time, specifically 80.1%. Considering this finding, we are convinced that there is ample scope for improvement. Thus, one of our forthcoming research areas will focus on optimizing the feature symbol search algorithm.

4. Conclusions

This article presents a sparse representation-based model for infrared polarization super-resolution reconstruction. We propose a method to overcome the limitations of the detector's sampling on the focal plane and achieve satisfactory results without requiring a large training set. Consequently, this approach is suitable for tasks where obtaining a vast amount of data is not feasible. Specifically, instead of independently solving each polarization angle, we solve the model on a designed Stokes vector field. This strategy effectively avoids errors caused by differential calculations during the polarization image-solving process. The simulation results depicted in Figure 3 demonstrate that our method effectively suppresses partial pseudo-polarization phenomena and generates more realistic polarization information compared to other existing methods. Furthermore, the results from a real test scene illustrated in Figure 5 reveal the significant advantages of our reconstruction results in object detection and classification tasks. Our algorithm delivers clearer edges of the targets and a noticeable contrast between the target and background, marking an improvement over the other algorithms discussed in this paper. In addition, to construct the dictionary set, we employ a self-developed detector to create a near-real-time short-wave infrared time-sharing polarization system. This system is equipped with a high-precision grating disk, enabling the continuous acquisition of polarization images. The main findings of our research are described in this article as follows:

(1) We propose a super-resolution reconstruction model for infrared polarization. (2) We design a reconstruction method based on the model. (3) We produce a prototype of a near-real-time short-wave infrared time-sharing polarization system and collect an infrared polarization dataset. (4) We build a short-wave infrared focal plane polarization system and conduct experiments to demonstrate the excellent results achieved by the proposed method in terms of quantitative measurement and visual quality.

In our future research, we intend to optimize the algorithms mentioned in the paper to enhance their speed in a software environment, with a primary focus on accelerating the feature symbol search algorithm. Moreover, we plan to integrate the proposed algorithm into our developed short-wave focal plane polarization detection system. Additionally, our future work involves incorporating convex optimization algorithms and deep learning methods to further improve image quality. Furthermore, we aim to explore the combination of metasurface design and its application in achieving full optical image reconstruction.

Author Contributions: Methodology, Y.M.; software, Y.M. and T.L.; validation, Y.M., S.W. and Z.Y.; formal analysis, S.W.; resources, F.L., S.W. and W.Q.; data curation, Y.M. and L.L.; writing—original draft preparation, Y.M.; writing—review and editing, F.L.; project administration, F.L. and L.L.; funding acquisition, F.L. and W.Q. All authors have read and agreed to the published version of the manuscript.

Funding: This research was funded by the National Pre-research Program during the 14th Five-Year Plan, grant number No. 514010405.

Institutional Review Board Statement: Not applicable.

Informed Consent Statement: Not applicable.

Data Availability Statement: Our data are derived from a self-developed time-sharing and focal-plane short-wave polarized infrared system. The system has been thoroughly refined and is now available for purchase. It encompasses imaging equipment, acquisition cards, an industrial computer, and software. Due to the inclusion of sensitive information, the dataset is not publicly accessible. Please reach out to the first author for the source code if necessary.

Conflicts of Interest: The authors declare no conflicts of interest.

Appendix A

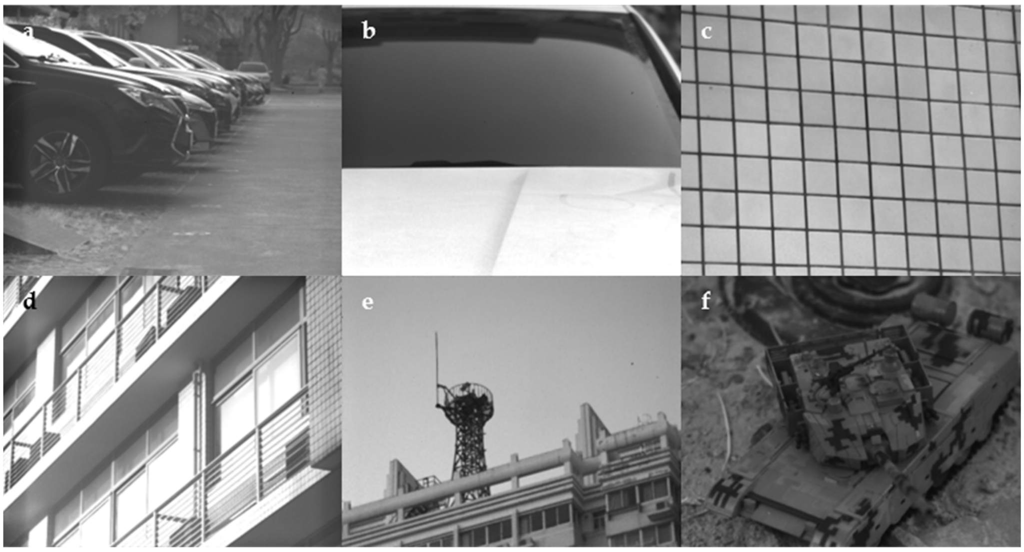

Figure A1. Simulation data strength diagram used for testing: (**a**) Cars, (**b**) Window, (**c**) Wall, (**d**) Building, (**e**) Tower, (**f**) Tank.

Table A1. Objective evaluation indexes of S0 results of different algorithms on different test images.

Method	Cars	Window	Wall	Building	Tank
EARI	SSIM = 0.4032 PSNR = 13.4202 RMSE = 0.2133	SSIM = 0.7799 PSNR = 14.5269 RMSE = 0.1878	SSIM = 0.4203 PSNR = 13.4207 RMSE = 0.2133	SSIM = 0.5723 PSNR = 21.7906 RMSE = 0.0814	SSIM = 0.3943 PSNR = 14.1210 RMSE = 0.1968
NP	SSIM = 0.4374 PSNR = 13.8023 RMSE = 0.2041	SSIM = 0.7858 PSNR = 14.6402 RMSE = 0.1854	SSIM = 0.4502 PSNR = 12.6379 RMSE = 0.2334	SSIM = 0.5519 PSNR = 21.5929 RMSE = 0.0832	SSIM = 0.4114 PSNR = 14.6783 RMSE = 0.1845
PCDP	SSIM = 0.4481 PSNR = 13.6557 RMSE = 0.2076	SSIM = 0.7918 PSNR = 14.7660 RMSE = 0.1827	SSIM = 0.4629 PSNR = 12.8692 RMSE = 0.2273	SSIM = 0.5441 PSNR = 19.9623 RMSE = 0.1004	SSIM = 0.4148 PSNR = 14.4895 RMSE = 0.1886
MPPOCS	SSIM = 0.6442 PSNR = 17.5827 RMSE = 0.1321	SSIM = 0.8353 PSNR = 15.7587 RMSE = 0.1630	SSIM = 0.6514 PSNR = 20.3389 RMSE = 0.0962	SSIM = 0.8971 PSNR = 36.8555 RMSE = 0.0144	SSIM = 0.6470 PSNR = 16.9773 RMSE = 0.1416
This Work	SSIM = 0.6966 PSNR = 18.0517 RMSE = 0.1252	SSIM = 0.8318 PSNR = 15.7436 RMSE = 0.1632	SSIM = 0.7093 PSNR = 20.8368 RMSE = 0.0908	SSIM = 0.9210 PSNR = 38.7827 RMSE = 0.0115	SSIM = 0.6933 PSNR = 17.3267 RMSE = 0.1360

Table A2. Objective evaluation indexes of S1 results of different algorithms on different test images.

Method	Cars	Window	Wall	Building	Tank
EARI	SSIM = 0.9637 PSNR = 39.6600 RMSE = 0.0104	SSIM = 0.9922 PSNR = 39.6600 RMSE = 0.0045	SSIM = 0.9195 PSNR = 37.5078 RMSE = 0.0133	SSIM = 0.8338 PSNR = 32.5971 RMSE = 0.0235	SSIM = 0.9886 PSNR = 46.5985 RMSE = 0.0047
NP	SSIM = 0.9806 PSNR = 42.4280 RMSE = 0.0076	SSIM = 0.9958 PSNR = 48.6937 RMSE = 0.0037	SSIM = 0.9639 PSNR = 40.3364 RMSE = 0.0096	SSIM = 0.8393 PSNR = 33.1142 RMSE = 0.0221	SSIM = 0.9931 PSNR = 48.0276 RMSE = 0.0040
PCDP	SSIM = 0.9781 PSNR = 41.7149 RMSE = 0.0082	SSIM = 0.9947 PSNR = 47.9808 RMSE = 0.0040	SSIM = 0.9498 PSNR = 39.1224 RMSE = 0.0111	SSIM = 0.8365 PSNR = 33.0923 RMSE = 0.0222	SSIM = 0.9916 PSNR = 47.3843 RMSE = 0.0042
MP	SSIM = 0.9938 PSNR = 48.9114 RMSE = 0.0036	SSIM = 0.9989 PSNR = 59.5889 RMSE = 0.0011	SSIM = 0.9984 PSNR = 58.3427 RMSE = 0.0012	SSIM = 0.9882 PSNR = 48.7383 RMSE = 0.0037	SSIM = 0.9986 PSNR = 58.9306 RMSE = 0.0011
This Work	SSIM = 0.9959 PSNR = 51.2608 RMSE = 0.0027	SSIM = 0.9991 PSNR = 60.5056 RMSE = 0.0010	SSIM = 0.9986 PSNR = 59.0080 RMSE = 0.0011	SSIM = 0.9926 PSNR = 51.1248 RMSE = 0.0028	SSIM = 0.9989 PSNR = 60.0059 RMSE = 0.0010

Table A3. Objective evaluation indexes of S2 results of different algorithms on different test images.

Method	Cars	Window	Wall	Building	Tank
EARI	SSIM = 0.9466 PSNR = 36.0382 RMSE = 0.0158	SSIM = 0.9909 PSNR = 45.3721 RMSE = 0.0055	SSIM = 0.9196 PSNR = 36.9036 RMSE = 0.0143	SSIM = 0.9356 PSNR = 37.7624 RMSE = 0.0129	SSIM = 0.9894 PSNR = 46.8909 RMSE = 0.0045
NP	SSIM = 0.9582 PSNR = 37.4198 RMSE = 0.01346	SSIM = 0.9933 PSNR = 46.3064 RMSE = 0.0048	SSIM = 0.9614 PSNR = 39.6867 RMSE = 0.0104	SSIM = 0.9518 PSNR = 39.1404 RMSE = 0.0110	SSIM = 0.9927 PSNR = 48.1039 RMSE = 0.0039
PCDP	SSIM = 0.9554 PSNR = 36.9204 RMSE = 0.01426	SSIM = 0.9930 PSNR = 46.1596 RMSE = 0.0049	SSIM = 0.9435 PSNR = 38.2077 RMSE = 0.0123	SSIM = 0.9518 PSNR = 38.9414 RMSE = 0.0113	SSIM = 0.9920 PSNR = 47.6478 RMSE = 0.0042
MP	SSIM = 0.9918 PSNR = 47.1006 RMSE = 0.0044	SSIM = 0.9983 PSNR = 56.4553 RMSE = 0.0015	SSIM = 0.9974 PSNR = 55.7543 RMSE = 0.0016	SSIM = 0.9706 PSNR = 42.0427 RMSE = 0.0079	SSIM = 0.9977 PSNR = 56.1393 RMSE = 0.0016
This Work	SSIM = 0.9948 PSNR = 49.6021 RMSE = 0.0033	SSIM = 0.9888 PSNR = 45.8931 RMSE = 0.0051	SSIM = 0.9981 PSNR = 57.6130 RMSE = 0.0013	SSIM = 0.9857 PSNR = 45.9872 RMSE = 0.0050	SSIM = 0.9965 PSNR = 53.0169 RMSE = 0.0022

Table A4. Objective evaluation indexes of DP results of different algorithms on different test images.

Method	Cars	Window	Wall	Building	Tank
EARI	SSIM = 0.8003 PSNR = 27.8272 RMSE = 0.0406	SSIM = 0.9442 PSNR = 30.8589 RMSE = 0.0287	SSIM = 0.6495 PSNR = 21.5937 RMSE = 0.0832	SSIM = 0.7586 PSNR = 26.9068 RMSE = 0.0452	SSIM = 0.6876 PSNR = 27.2853 RMSE = 0.0432
NP	SSIM = 0.8284 PSNR = 29.3589 RMSE = 0.0340	SSIM = 0.9419 PSNR = 30.6841 RMSE = 0.0292	SSIM = 0.6942 PSNR = 24.7070 RMSE = 0.0582	SSIM = 0.7590 PSNR = 27.8181 RMSE = 0.0407	SSIM = 0.7227 PSNR = 28.3058 RMSE = 0.0384
PCDP	SSIM = 0.8216 PSNR = 28.9635 RMSE = 0.0356	SSIM = 0.9484 PSNR = 31.2784 RMSE = 0.0273	SSIM = 0.6709 PSNR = 22.9016 RMSE = 0.0716	SSIM = 0.7798 PSNR = 28.0442 RMSE = 0.0396	SSIM = 0.7113 PSNR = 27.7868 RMSE = 0.0408

Table A4. *Cont.*

Method	Cars	Window	Wall	Building	Tank
MP	SSIM = 0.9496 PSNR = 36.8699 RMSE = 0.0143	SSIM = 0.9747 PSNR = 40.9748 RMSE = 0.0089	SSIM = 0.9682 PSNR = 44.0480 RMSE = 0.0063	SSIM = 0.9293 PSNR = 36.1728 RMSE = 0.0155	SSIM = 0.9213 PSNR = 37.4231 RMSE = 0.0135
This Work	SSIM = 0.9653 PSNR = 40.6423 RMSE = 0.0093	SSIM = 0.9496 PSNR = 31.4468 RMSE = 0.0268	SSIM = 0.9775 PSNR = 45.8423 RMSE = 0.0051	SSIM = 0.9599 PSNR = 39.6173 RMSE = 0.0105	SSIM = 0.9338 PSNR = 35.5246 RMSE = 0.0167

Table A5. Objective evaluation indexes of AP results of different algorithms on different test images.

Method	Cars	Window	Wall	Building	Tank
EARI	SSIM = 0.9665 PSNR = 31.4232 RMSE = 0.0268	SSIM = 0.9834 PSNR = 41.2151 RMSE = 0.0087	SSIM = 0.9616 PSNR = 31.9594 RMSE = 0.0252	SSIM = 0.9223 PSNR = 27.5346 RMSE = 0.0420	SSIM = 0.9788 PSNR = 41.9182 RMSE = 0.0080
NP	SSIM = 0.9740 PSNR = 32.7683 RMSE = 0.0230	SSIM = 0.9848 PSNR = 42.4306 RMSE = 0.0076	SSIM = 0.9665 PSNR = 33.1721 RMSE = 0.0220	SSIM = 0.9477 PSNR = 29.4241 RMSE = 0.0338	SSIM = 0.9834 PSNR = 43.2909 RMSE = 0.0069
PCDP	SSIM = 0.9752 PSNR = 32.8784 RMSE = 0.0227	SSIM = 0.9859 PSNR = 42.6716 RMSE = 0.0074	SSIM = 0.9696 PSNR = 33.6649 RMSE = 0.0207	SSIM = 0.9484 PSNR = 29.4233 RMSE = 0.0338	SSIM = 0.9848 PSNR = 43.6527 RMSE = 0.0066
MP	SSIM = 0.9725 PSNR = 32.2656 RMSE = 0.0244	SSIM = 0.9852 PSNR = 41.3038 RMSE = 0.0086	SSIM = 0.9675 PSNR = 32.7580 RMSE = 0.0230	SSIM = 0.9335 PSNR = 27.6061 RMSE = 0.0417	SSIM = 0.9818 PSNR = 42.0923 RMSE = 0.0079
This Work	SSIM = 0.9845 PSNR = 34.7240 RMSE = 0.0184	SSIM = 0.9892 PSNR = 46.0793 RMSE = 0.0050	SSIM = 0.9810 PSNR = 37.4299 RMSE = 0.0134	SSIM = 0.9757 PSNR = 33.1091 RMSE = 0.0221	SSIM = 0.9918 PSNR = 46.8903 RMSE = 0.0045

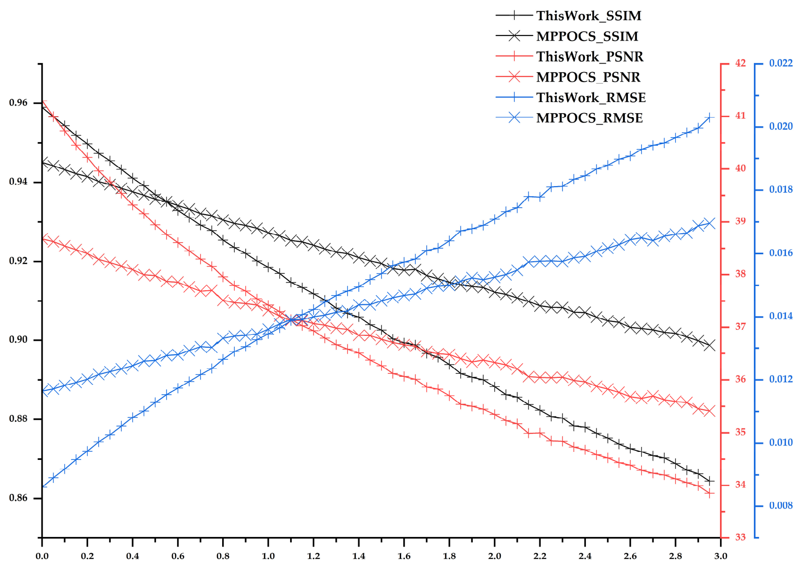

Figure A2. The objective evaluation indexes of our algorithm and MPPOCS in the tower dataset on AP images under different noise conditions.

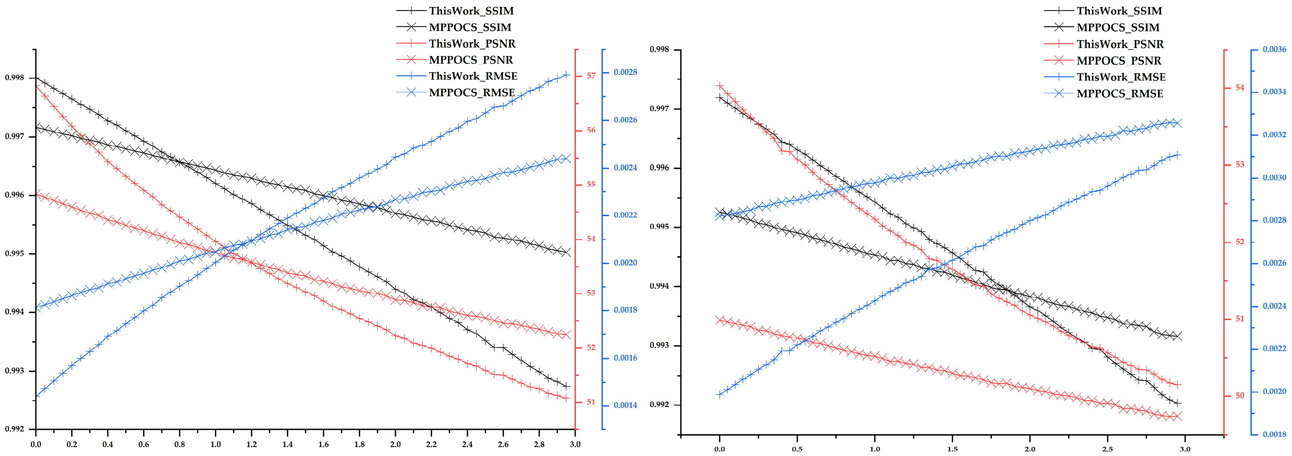

(**a**) (**b**)

Figure A3. The objective evaluation indexes of our algorithm and MPPOCS for a tower, as measured under varying noise conditions: (**a**) Objective evaluation indexes of S1, (**b**) Objective evaluation indexes of S2.

References

1. Rosenberger, M.; Horn, R.; Golomoz, A.; Dittrich, P.-G.; Illmann, R.; Fütterer, R.; Notni, G. Investigation on surface inspection using polarizing image sensors. In Proceedings of the Image Sensing Technologies: Materials, Devices, Systems, and Applications IX, SPIE, Orlando, FL, USA, 30 May 2022; Volume 12091, pp. 113–125.
2. Schommer, D.; Duhovic, M.; Hoffmann, T.; Ernst, J.; Schladitz, K.; Moghiseh, A.; Gortner, F.; Hausmann, J.; Mitschang, P.; Steiner, K. Polarization imaging for surface fiber orientation measurements of carbon fiber sheet molding compounds. *Compos. Commun.* **2023**, *37*, 101456.
3. Xu, C.; Zheng, D.; Huang, Y.; Zeng, Z. Defect inspection of optical components based on dark-field polarization imaging and convolutional neural network recognition algorithms. *Opt. Eng.* **2023**, *62*, 043101.
4. Zhao, Y.; Reda, M.; Feng, K.; Zhang, P.; Cheng, G.; Ren, Z.; Kong, S.G.; Su, S.; Huang, H.X.; Zang, J. Detecting giant cell tumor of bone lesions using Mueller matrix polarization microscopic imaging and multi-parameters fusion network. *IEEE Sens. J.* **2020**, *20*, 7208–7215. [CrossRef]
5. Ahmad, I.; Khaliq, A.; Iqbal, M.; Khan, S. Mueller matrix polarimetry for characterization of skin tissue samples: A review. *Photodiagn. Photodyn. Ther.* **2020**, *30*, 101708. [CrossRef]
6. Rahaman, A.; Anantharaju, A.; Jeyachandran, K.; Manideep, R.; Pal, U.M. Optical imaging for early detection of cervical cancer: State of the art and perspectives. *J. Biomed. Opt.* **2023**, *28*, 080902.
7. Tauc, M.J.; Rehbein, E.M.; Eshelman, L.M.; Shaw, J.A. Polarization enhancement of passive SWIR cloud thermodynamic phase remote sensing. In Proceedings of the Polarization Science and Remote Sensing IX, SPIE, San Diego, CA, USA, 6 September 2019; Volume 11132, pp. 25–33.
8. Chen, W.; Yan, L.; Chandrasekar, V. Optical polarization remote sensing. *Int. J. Remote Sens.* **2020**, *41*, 4849–4852.
9. Wang, H.; Zhang, P.; Yin, D.; Li, Z.; Shang, H.; Xu, H.; Shang, J.; Gu, S.; Hu, X. Shortwave Infrared Multi-Angle Polarization Imager (MAPI) Onboard Fengyun-3 Precipitation Satellite for Enhanced Cloud Characterization. *Remote Sens.* **2022**, *14*, 4855. [CrossRef]
10. Huang, H.; Yu, Y.; Li, X.; Sun, D.; Zhang, G.; Li, T.; Shao, X.; Yang, B. Shortwave Infrared InGaAs Detectors On-Chip Integrated with Subwavelength Polarization Gratings. *Nanomaterials* **2023**, *13*, 2512. [CrossRef]
11. Zhang, J.C.; Chen, J.L.; Luo, H.B. Polarization image interpolation algorithm based on tensor non-negative sparse decomposition. *Acta Opt. Sin.* **2021**, *41*, 1411001.
12. Gao, S.; Gruev, V. Bilinear and bicubic interpolation methods for division of focal plane polarimeters. *Opt. Express* **2011**, *19*, 26161–26173. [CrossRef]
13. Gao, S.; Gruev, V. Gradient-based interpolation method for division-of-focal-plane polarimeters. *Opt. Express* **2013**, *21*, 1137–1151. [CrossRef]
14. Li, N.; Zhao, Y.; Pan, Q.; Kong, S.G. Demosaicking DoFP images using Newton's polynomial interpolation and polarization difference model. *Opt. Express* **2019**, *27*, 1376–1391. [CrossRef] [PubMed]
15. Morimatsu, M.; Monno, Y.; Tanaka, M.; Okutomi, M. Monochrome and color polarization demosaicking based on intensity-guided residual interpolation. *IEEE Sens. J.* **2021**, *21*, 26985–26996. [CrossRef]
16. Wu, R.; Zhao, Y.; Li, N.; Kong, S.G. Polarization image demosaicking using polarization channel difference prior. *Opt. Express* **2021**, *29*, 22066–22079. [CrossRef]

17. Chen, J.; Wang, W.G.; Liu, T.X.; Zhang, Z.D.; Gao, H.B. A POCS super resolution restoration algorithm based on BM3D. *Sci. Rep.* **2017**, *7*, 15049. [CrossRef] [PubMed]
18. Zhang, X.F.; Huang, W.; Xu, M.F.; Jia, S.Q.; Xu, X.R.; Li, F.B.; Zheng, Y.D. Super-resolution imaging for infrared micro-scanning optical system. *Opt. Express* **2019**, *27*, 7719–7737. [CrossRef]
19. Ma, Y.; Wang, S.; Lei, T.; Li, B.; Li, F. Super-resolution reconstruction of focal plane infrared polarization microscan images. *Opt. Precis. Eng.* **2023**, *31*, 2418–2429. [CrossRef]
20. Zhang, J.; Shao, J.; Luo, H.; Zhang, X.; Hui, B.; Chang, Z.; Liang, R. Learning a convolutional demosaicing network for microgrid polarimeter imagery. *Opt. Lett.* **2018**, *43*, 4534–4537.
21. Zeng, X.; Luo, Y.; Zhao, X.; Ye, W. An end-to-end fully-convolutional neural network for division of focal plane sensors to reconstruct s 0, dolp, and aop. *Opt. Express* **2019**, *27*, 8566–8577. [CrossRef]
22. Xu, G.; Wang, J.; Zhang, L.; Ma, J.; Wang, Y.; Liu, J. Multi-scale adaptive weighted network for polarization computational imaging super-resolution. *Appl. Phys. B* **2022**, *128*, 200. [CrossRef]
23. Xu, M.; Wang, C.; Wang, K.; Shi, H.; Li, Y.; Jiang, H. Polarization Super-Resolution Imaging Method Based on Deep Compressed Sensing. *Sensors* **2022**, *22*, 9676. [CrossRef] [PubMed]
24. Liu, J.; Duan, J.; Hao, Y.; Chen, G.; Zhang, H.; Zheng, Y. Polarization image demosaicing and RGB image enhancement for a color polarization sparse focal plane array. *Opt. Express* **2023**, *31*, 23475–23490. [CrossRef]
25. Wen, S.; Zheng, Y.; Lu, F.; Zhao, Q. Convolutional demosaicing network for joint chromatic and polarimetric imagery. *Opt. Lett.* **2019**, *44*, 5646–5649. [PubMed]
26. Wen, S.; Zheng, Y.; Lu, F. A sparse representation based joint demosaicing method for single-chip polarized color sensor. *IEEE Trans. Image Process.* **2021**, *30*, 4171–4182. [PubMed]
27. Zhang, J.; Chen, J.; Yu, H.; Yang, D.; Liang, B.; Xing, M. Polarization image demosaicking via nonlocal sparse tensor factorization. *IEEE Trans. Geosci. Remote Sens.* **2021**, *60*, 5607210.
28. Zhang, J.; Luo, H.; Liang, R.; Ahmed, A.; Zhang, X.; Hui, B.; Chang, Z. Sparse representation-based demosaicing method for microgrid polarimeter imagery. *Opt. Lett.* **2018**, *43*, 3265–3268. [PubMed]
29. Ma, Y.; Wang, S.; Lei, T.; Li, B.; Li, F. Imaging model and error analysis of quasi-real-time polarization detection system based on continuous rotation. *Optoelectron. Technol. Appl.* **2022**, *37*, 82–87+102.
30. Chang, H.; Yeung, D.Y.; Xiong, Y. Super-resolution through neighbor embedding. In Proceedings of the 2004 IEEE Computer Society Conference on Computer Vision and Pattern Recognition 2004, CVPR 2004, Washington, DC, USA, 27 June–2 July 2004; IEEE: Piscataway, NJ, USA, 2004; Volume 1, p. I.
31. Zhu, Z.; Li, X.; Zhang, J.; Zhou, Y.; Zhao, Y. Specular flare suppression method for reflective materials based on the optimal polarizing angle. *Appl. Opt.* **2022**, *61*, 8034–8041. [CrossRef]
32. Lee, H.; Battle, A.; Raina, R.; Ng, A. Efficient sparse coding algorithms. *Adv. Neural Inf. Process. Syst.* **2006**, *19*, 801–808.
33. Olshausen, B.A.; Field, D.J. Sparse coding with an overcomplete basis set: A strategy employed by V1? *Vis. Res.* **1997**, *37*, 3311–3325. [CrossRef]
34. Ma, Y.; Li, X.; Shao, X.; Deng, S.; Cheng, J.; Gu, Y.; Liu, Y.; Chen, Y.; Zhu, X.; Li, T.; et al. 320 $\times$ 256 Extended Wavelength $In_xGa_{1-x}As$/InP Focal Plane Arrays: Dislocation Defect, Dark Signal and Noise. *IEEE J. Sel. Top. Quantum Electron.* **2021**, *28*, 3800411.